Impact of autistic-derived metabolites on the dynamics and connectivity of neuronal cultures

Author: Sarah Gómez García*
Master en Física dels Sistemes Complexos i Biofísica.
Facultat de Física, Universitat de Barcelona, Martí i Franquès 1, 08028 Barcelona, Spain.†

Advisor: Jordi Soriano Fradera
(Dated: June 30, 2025)

Autism spectrum disorder (ASD) is a neurodevelopmental condition with complex and largely unknown causes. While genetic factors are widely studied, growing evidence suggests that environmental influences, including gut microbiome alterations, may play a significant role in ASD pathophysiology. Recent hypotheses propose that disruptions in gut microbiota composition could impact brain function and contribute to the development of ASD. This study investigates the effects of ASD-associated microbiota metabolites on the dynamics and connectivity of neuronal cultures, which provide an accessible model to explore brain-like processes at the cellular level, offering insights into how neuronal abnormalities may lead to dysfunction and disease. To examine this, three types of cultures are analyzed: cultures treated with fecal-derived metabolites from individuals with ASD or neurotypical individuals, and control cultures. All samples contain metabolites that differentially influence neuronal behavior. Experimental data is combined with an *in silico* model to help understanding the relationship between neuron-level connectivity and network-wide collective behavior. Results show that ASD cultures exhibit alterations in spontaneous activity and effective connectivity as compared to the neurotypical condition, although these alterations are not preserved along development, an aspect that hints at the activation of plasticity mechanisms that counterbalance possible damage By elucidating the effects of ASD-associated microbiota metabolites on neuronal function, this study helps advance our understanding of gut-brain interactions in ASD and their role in neurodevelopmental disorders.

I. INTRODUCTION

Autism spectrum disorder (ASD), also known as autism, is a neurodevelopmental disorder that describes a set of social communication deficits, repetitive and sensory behaviors, and/or highly restricted interests that appear in early childhood [1]. ASD has a worldwide prevalence of approximately 1%, making it one of the most common pervasive developmental disorders [2].

ASD is thought to be the product of overall brain reorganization in early developmental stages. Several studies have associated this neurodevelopmental disorder with subtle malformations, such as changes in cerebellar architecture and connectivity [2], and neural circuit alterations [3]. One of the most widely accepted examples of these neuroanatomical anomalies is an overgrowth of brain volume in early childhood and infancy. Contrary to neurotypically developing individuals, children with autism present an accelerated development of the brain, resulting in altered connectivity. However, ASD brain physiology is complex and, usually, research on ASD finds patterns of general brain under-connectivity combined with focal over-connectivity within specific regions [4].

In this regard, research in ASD has mostly focused at a brain level. Indeed, functional Magnetic Resonance Imaging (fMRI) is a high-resolution non-invasive technique that can help understand how the brain structurally and functionally develops in various brain diseases, including autism [5, 6]. ASD studies based on fMRI, aim at constructing the functional connectivity (FC) —defined as correlated neural activity between brain regions [6]— from the blood oxygenation level-dependent signal (BOLD) [5]. In particular, resting state (RS) fMRI is able to detect the changes in hemodynamics necessary to support neural activity when the brain is "at rest", i.e. no specific task is being performed [6]. During this state, the brain exhibits a high degree of functional connectivity, known as intrinsic connectivity [3]. It is important to note that findings in ASD populations have been heterogeneous, likely due to differences in methodological approaches, analysis techniques and the intrinsic variability of the disorder, among others [6]. Despite these inconsistencies, altered intrinsic connectivity within the default network is a recurring observation in ASD cohorts [3]. The nature of these alterations remains a subject of ongoing debate, as both hypo-connectivity and hyper-connectivity, as well as region-specific combinations of the two, have been reported across studies [7, 8]. While a majority of RS-fMRI investigations point to reduced local or long-range FC in individuals with ASD relative to neurotypical controls [6], some have also documented increases in connectivity between certain brain regions [8].

Although no comprehensive explanation has been found for the causation of ASD, it is understood that autism is a neurobiological disorder influenced by genetic

* sgomezga23@alumnes.ub.edu
† master.complex.biophys@ub.edu

and environmental factors [2]. In fact, autism has been associated with abnormalities in the gut microbiota (gut dysbiosis) and exposure to neurotoxins [9].

From a biological point of view, the brain and gut are tightly connected through a complex, bidirectional communication system known as the 'gut-brain axis' (GBA). The gut microbiota is a diverse ecosystem, composed by bacteria, archea, fungi and viruses found in the gastrointestinal tract of animals, i.e. the hosts. Through experimentation with germ-free animals, it has been proven that even though the gut-microbiome is non-essential, it plays a key role in normative aspects of host development and physiology. For instance, it has several protective roles, such as protection against pathogens, infections, auto-immunity, auto-inflammation and disease [10]. When considering the effects of microbes on human health, processes are believed to be regulated to maintain healthy microbiome-host interactions for the host, and deviation from these health-state interactions result in illness [11].

Alterations in the gut microbial community have been proposed to influence cognitive and behavioral functions, as well as brain physiology, through the GBA [12]. Emerging evidence has linked disruptions in gut microbial homeostasis, namely, gut dysbiosis, to ASD [13], prompting hypotheses regarding its potential role in the disorder's causation. One proposed mechanism involves the increased neurotoxin absorption through the gut wall into the circulatory system as a result of dysbiosis-induced barrier dysfunction. Under conditions of increased intestinal permeability, certain neurotoxic metabolites may reach concentrations sufficient to penetrate a compromised blood–brain barrier (BBB), potentially triggering neurodevelopmental alterations. This risk may be heightened during early postnatal development, a period in which the BBB has not yet reached full functional maturity. Consequently, early-onset gut dysbiosis may facilitate the systemic dissemination of neurotoxins, thereby increasing the likelihood of their entry into the circulatory system and brain, initiating neurodevelopmental damage [14].

As previously noted, investigating ASD directly in the human brain, i.e. *in vivo*, presents significant challenges. To address this limitation, the present study adopts an alternative strategy based on *in vitro* neuronal cultures. *In vitro* neuronal cell cultures have proven to be powerful experimental tools as they provide accessible and malleable models for brain-like processes and their alterations [15]. For this reason, cultures are widely used in diverse fields such as medicine, bioengineering, mathematics, and physics of complex systems [16]. In particular, understanding how neurons work at the cellular level can help elucidate how abnormalities in their interactions can lead to brain dysfunction and disease [17].

Thus, the project at hand aims to investigate how the presence of autistic-derived metabolites alters the connectivity of *in vitro* neuronal networks, and in turn, shapes its dynamics. To this end, three types of cultures are analyzed: cultures treated with fecal-derived metabolites from individuals with ASD, cultures treated with fecal-derived metabolites from neurotypical individuals, and untreated control cultures. Each fecal extract contains bioactive compounds capable of modulating neuronal activity. The primary objective is to characterize how ASD-associated microbial metabolites influence network-level neuronal function, thereby contributing to a deeper understanding of gut-brain interactions and their relevance to neurodevelopmental disorders.

II. EXPERIMENTAL METHODS

A. Collection of fecal samples

Recent studies have shown that more than 98% of the human microbiota resides in the most distal region of the gut, namely the colon. In this way, fecal samples, which are widely used for the analysis of the human gut microbiota, are representative of the most abundant microbial communities in our bodies and their impact on human health [18].

Two human fecal samples provided by the "Instituto Ramón y Cajal de Investigación Sanitaria (IRYCIS, Madrid, Spain)" were used in this study, one from an individual with autism and the other from a neurotypical person, i.e. a subject that did not have autism or any other neurodivergence. To process the samples, the fecal matter was first lyophilized and then diluted in phosphate-buffered saline (PBS) to a final concentration of 60 mg/mL. The resulting mixture was centrifuged at 3000 g for 20 minutes, and the supernatant was subsequently filtered using a 0.22 μm pore size polyethersulfone membrane filter. The final preparations consisted of sterile PBS solutions containing metabolites derived from the host-associated microbiota. To preserve metabolite integrity, all samples were stored at approximately -18°C until use.

B. Neuronal culture preparation

Homogeneous cortical neuron cultures were prepared from Sprague-Dawley rat embryos and seeded on glass coverslips that contained a poly-dimethylsiloxane (PDMS) ring, which allowed to confine the neurons in a predefined field of view (Fig. 1A). Three types of cultures were prepared: one treated with autistic fecal matter, another treated with non-autistic (neurotypical) fecal matter, and a third without fecal matter, i.e. the control.

Prior to dissection, PDMS rings with an internal diameter of 10 mm were affixed to 13 mm glass coverslips using an oxygen plasma treatment to promote bonding. Oxygen plasma exposure enhances the adhesion properties of PDMS and glass [19], and was employed to ensure a stable and durable bond between the ring and the coverslip. Neuronal cultures were subsequently grown on

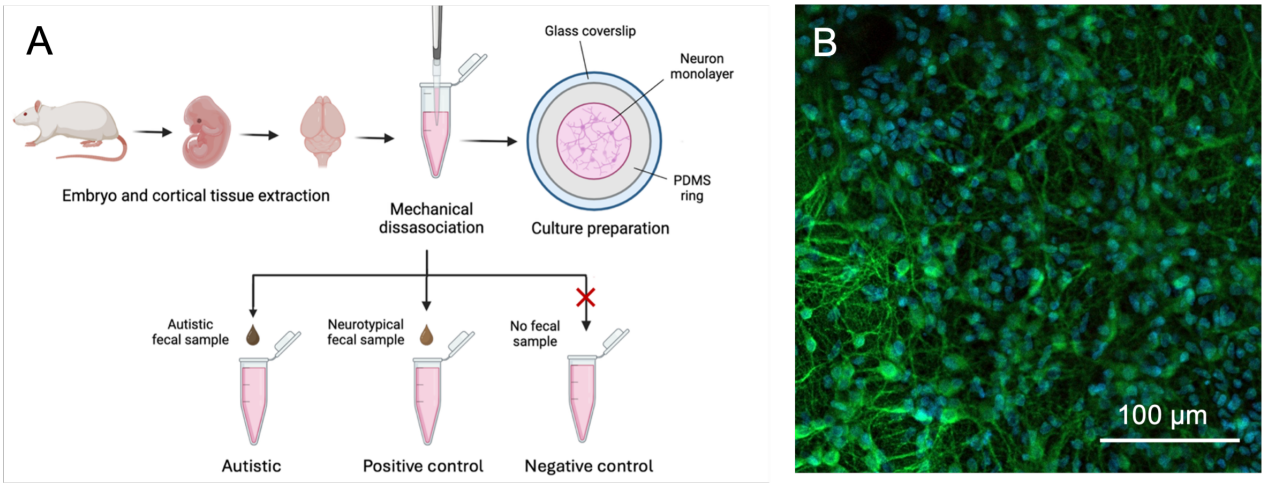

FIG. 1. (**A**) Schematic representation of the main experimental procedures used to obtain the neuronal cultures, including cortical tissue extraction, mechanical dissociation, injury induction, and cell seeding. Illustration created with *BioRender.com*. (**B**) Representative immunofluorescence image of a 1:200 neurotypical culture fixed at day *in vitro* 7. Cell membranes and neurites (axons and dendrites) are labeled in green; nuclei are stained in blue.

the glass surface, confined within the area defined by the PDMS ring. To ensure sterility, the assembled PDMS-glass substrates were autoclaved 24 hours prior to dissection. Following sterilization, each substrate was placed into a well of a 4-well plate and incubated overnight with a poly-L-lysine (PLL) solution, which enhances neuronal adhesion [20]. However, due to its cytotoxicity, the substrates were thoroughly rinsed prior to cell seeding to remove any residual unbound PLL.

As sketched in Fig. 1A, on the day of dissection, rat embryos were harvested, and their brains and cortices were extracted. The embryonic cortical tissue was then mechanically dissociated and suspended in plating medium. Following dissociation, cell concentration was determined using a Neubauer hemocytometer in conjunction with trypan blue staining to assess cell viability. Based on the calculated concentration, the cell suspension was diluted to achieve a final density of 3000 neurons/mm^2. The resulting cell suspension was seeded within the PDMS ring to confine the neurons to the defined 10 mm diameter area. Cultures were incubated for approximately two hours to allow neuronal sedimentation and adhesion. After this period, additional plating medium was added to reach a final volume of 1 mL.

To simulate potential pathological conditions, cultures were subsequently treated with diluted fecal samples from both autistic and neurotypical donors. The fecal samples, were added to the cultures at final dilutions of 1:200 and 1:500 relative to the original PBS-fecal matter solution. Finally, neuronal cultures were infected with an adeno-associated virus (AAV) encoding for the fluorescence calcium indicator GCaMP6s, enabling fluorescence-based monitoring of neuronal activity. All cultures contained a mixed population of 80% excitatory neurons and 20% inhibitory neurons. Spontaneous activity in cultures was detectable by day *in vitro* (DIV) 7 and was subsequently recorded at DIV 7, 10, 12, and 14 to monitor its evolution over time.

Since neurotoxic action is expected to primarily affect the capacity of the neuronal culture to form a network, which mostly occurs during the 48h after plating, we opted to change or refresh the medium throughout the culture period. Thus, culture medium was changed periodically (every 3 days) to ensure optimal conditions. All cultures were maintained in a humidified incubator at 95% relative humidity, 37°C, and 5% CO_2.

C. Immunostaining

Immunostaining is an essential technique in biological research that utilizes the principle of antigen-antibody interaction to visualize specific molecules within cells or tissues with assistance of florescence markers. Essentially, immunostaining is based on the specificity of binding between an antibody (carrying a fluorescent dye) and its target antigen [21]. By combining antibodies with fluorescence dyes of different excitation/emission wavelengths ("colors") it is possible to identify the presence of specific proteins in the neuronal network.

For this study, basic immunofluorescence staining was performed on neuronal cultures using a combination of fluorophores: Alexa Fluor 488 (green) to label neuronal structures, including axons and dendrites, and DAPI (blue) to stain cell nuclei. An example for the neurotypical case is shown in Fig. 1B. In general, no substantial structural differences were observed under the 3 conditions, indicating that more precise staining targeting proteins associated with synapse formation must be performed to identify connectivity-related alterations.

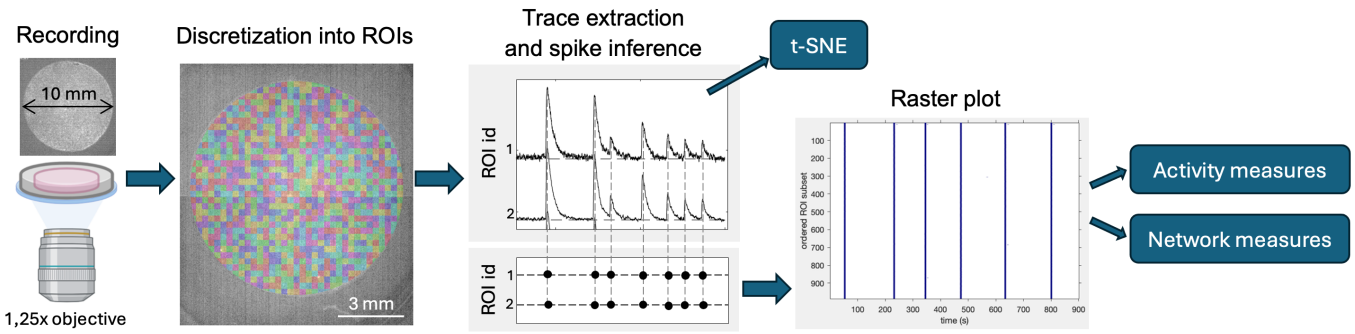

FIG. 2. Data analysis pipeline comprised of the following steps: acquisition of the fluorescence imaging recordings, discretization with a 35×35 circular grid, fluorescence trace extraction, which will be used for the t-SNE analysis, and finally, spike inference to build the raster plot, which will be used to extract both the activity and network measures.

III. DATA ANALYSIS

A. Fluorescence imaging and GCaMP6s calcium probe

Spontaneous neuronal activity was tracked using fluorescence calcium imaging. This technique relies on the use of calcium-activated fluorescence sensors to visualize the rapid increase in intracellular Ca^{2+} levels during cellular communication. It is known that when action potentials flow through neurons, they activate voltage-gated calcium channels that transport Ca^{2+} into the cytoplasm. In turn, this process triggers the emission of neurotransmitters into the synaptic cleft, propagating the activation to connected neurons. Therefore, since intracellular calcium levels and synapse propagation are closely related, calcium sensors are excellent tools for the study of neuronal activity.

Our calcium-sensitive compound, GCaMP6s, is a protein-based genetically encoded calcium indicator (GECI). This compound is packed into an AAV viral particle, and once the neurons are infected by the virus they express the indicator, as long as they are alive [16]. In the presence of Ca^{2+}, the GCaMP6s molecule undergoes a conformational change, the chromophore inside becomes stabilized, and it gives off fluorescence [22]. The emitted radiation can then be measured with a fluorescence camera attached to a high-resolution microscope. Neuronal cultures were recorded at 33 fps for 15 minutes.

Obtained data was analyzed using a MATLAB-built software named NETCAL ('NETwork and population dynamics analysis of CALcium imaging recording'), developed by Javier G. Orlandi in 2018. NETCAL was designed to analyze high-resolution high-speed calcium imaging experiments [23].

Following video acquisition and initial preprocessing in NETCAL, the data were discretized into regions of interest (ROIs) by applying a 35×35 circular grid, yielding a total of 989 ROIs per experiment (Fig. 2). For each ROI, the software extracted and smoothed fluorescence time series (traces) representing the average fluorescence intensity as a function of time.

To further process the data, spike inference was applied. Specifically, Schmitt trigger-based inference was used to assign a binary value to each ROI at each time point: if activity is detected the ROI is assigned with the value '1' at time t, or '0' otherwise. The resulting binary activity patterns were visualized in raster plots, where each dot corresponds to an active ROI at time t. The presence of apparent vertical alignments in these plots reflects the occurrence of collective activity events (*network bursts*) that propagate rapidly —on the order of a few milliseconds— across the entire network. The general data analysis pipeline is schematically summarized in Fig. 2.

B. Activity descriptors

Subsequently, the propagation velocity of activity fronts was quantified using custom-built software tools developed in Dr. Soriano's lab. Assuming a circular propagation of the fronts, the software analyzes global firing events and computes the propagation velocity for each event, as shown in Fig. 3.

As demonstrated both experimentally and theoretically by Jacobi *et al.* (2010), the velocity of activity front propagation strongly depends on the average connectivity of the neuronal network and the balance between excitation and inhibition [24]. Thus, analyzing the propagation velocity offers a valuable indirect approach to gain insight on the connectivity of neuronal cultures and assess how it evolves during development or in response to damage [16].

An additional metric used to evaluate network activity is the total number of firing events per ROI. Specifically, an ROI is considered active if it exhibits at least two firing events (e), corresponding to a threshold of $e \geq 2$. By analyzing the distribution of firing events across all ROIs, one can assess the overall behavioral activity patterns of the system.

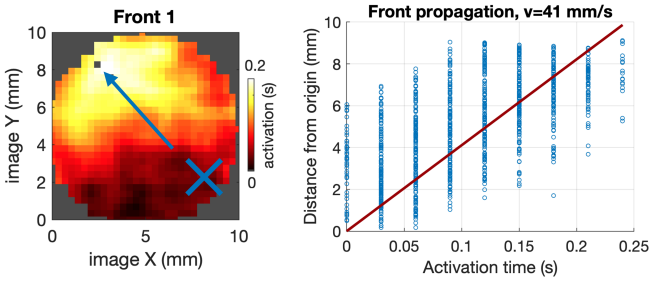

FIG. 3. (Left) Front propagation, where the cross is the origin, and the blue arrow the direction of propagation. (Right) Distance from the origin to the front as a function of time, with its corresponding linear regression.

C. Effective connectivity inference

Effective connectivity was inferred from spontaneous calcium fluorescence activity using the generalized transfer entropy (GTE) framework [25]. Spike trains were binarized over a 15-minute recording period, assigning a value of '1' to time bins containing a spike and '0' otherwise, with a temporal resolution of 30 ms. A directed connection from ROI i to ROI j ($TE_{i\to j}$) was identified when the inclusion of activity from ROI i significantly enhanced the predictability of future states of j.

To assess statistical significance, a z-score was computed by comparing each estimated transfer entropy value to the empirical distribution derived from all possible input-output pairings, defined as:

$$z = \frac{TE_{i\to j} - \langle TE_{\text{joint}} \rangle}{\sigma_{\text{joint}}}, \tag{1}$$

where TE_{joint} denotes the mean and σ_{joint} the standard deviation of the joint transfer entropy distribution.

A threshold of $z = 2$ was adopted to determine significance, as this value provided an optimal balance for detecting both global and local patterns of information transfer. Connections exceeding this threshold were accepted as significant and binarized such that the effective connectivity matrix $\mathbf{A} = \{a_{ij}\}$ consisted of directed, unweighted links with $a_{ij} = 1$ for the significant connection and $a_{ij} = 0$ otherwise.

D. Connectivity descriptors

Network science provides a powerful framework for describing interconnected systems as an ensemble of nodes and their interactions through edges. In neuroscience, nodes typically correspond to individual neurons or regions of interest (ROIs), while edges may denote either (i) *structural* connections, such as axonal projections, or (ii) *functional* connections defined by statistical relationships between the activity time series of different nodes [26]. A further refinement may include *effective* connections, which correspond to causal (directed) interactions between neuronal activation. Similarly to the brain, neuronal cultures are physically-embedded systems with intrinsic directionality given by axonal projections. As such, spatial constraints combined with directionality play a fundamental role in shaping the architecture of the resulting networks [26]. To investigate the directional flow of information within such systems, the aforementioned effective connectivity can be computed using information-theoretic measures such as transfer entropy. Unlike functional connectivity, which captures undirected statistical associations, effective connectivity reflects directed, potentially causal interactions among nodes and is thought to provide a more accurate representation of information transmission in neuronal networks [27].

The degree of a node, k, is defined as the number of connections associated with that node [26]. In a directed network represented by a binary adjacency matrix $\mathbf{A} = \{a_{ij}\}$ where $a_{ij} = 1$ indicates a directed *effective* connection from ROI i to ROI j, and $a_{ij} = 0$ the absence of a connection, the degree of node i is given by:

$$k_i = \sum_{j\in N} a_{ij}. \tag{2}$$

Here, N is the total number of nodes. Since the adjacency matrix is directed and therefore asymmetric, the total degree k_i can be decomposed into two components: the in-degree, defined as $k_j^{in} = \sum_{i\in N} a_{ij}$, and the out-degree, given by $k_i^{out} = \sum_{j\in N} a_{ij}$. Consequently, the total degree of a neuron i is expressed a $k_i = k_i^{in} + k_i^{out}$ [28]. In this way, the average degree of the network can be computed as the average of k_i over all nodes in the network:

$$\langle k \rangle = \sum_{i\in N} k_i. \tag{3}$$

Functional segregation in complex networks is often quantified using *modularity*, a measure introduced by Newman and Girvan in 2004 [29]. Modularity, Q, represents the existence of densely connected groups of nodes, with sparser connections between groups. Essentially, it is computed as the number of edges falling within groups minus the expected number in an equivalent network with edges placed at random [30]. Mathematically, it can be expressed as:

$$Q = \frac{1}{2m} \sum_{ij} \left(a_{ij} - \frac{k_i k_j}{2m} \right) \delta(C_i, C_j), \tag{4}$$

where m is the number of edges, a_{ij} the element of the effective connectivity adjacency matrix, k_i, k_i denotes the degrees of the i-th and j-th nodes respectively and $\delta(C_i, C_j)$ is the Kronecker delta, equal to 1 if nodes i and j belong to the same community and 0 otherwise. The term $\frac{k_i k_j}{2m}$ represents the expected number of edges between vertices i and j if edges are placed

at random [31]. Therefore, high values of Q indicate a pronounced community structure and greater functional segregation, while lower values suggest a more integrated network organization. Community structure was identified by optimizing modularity using the Louvain algorithm, a widely adopted algorithm for detecting communities in large networks [25].

Functional integration is commonly assessed using *global efficiency*, which reflects the network's ability to process information [32]. Global efficiency, G_{eff}, is defined as the average inverse shortest path length between all pairs of nodes [28] in the, connectivity matrix, effective connectivity in our case, and is given by:

$$G_{\text{eff}} = \frac{1}{N(N-1)} \sum_{i \neq j} \frac{1}{d_{ij}}, \tag{5}$$

where N is the number of nodes and d_{ij} is the topological distance between two nodes [32]. Global efficiency ranges between 0 (the network is completely disconnected) and 1 (fully interconnected or 'complete graph').

E. Autoencoder

Autoencoders are a class of unsupervised artificial neural network algorithms designed to reconstruct its input by learning a compact latent representation of the original data. Architecturally, they are characterized by an equal number of input and output layers, with a central bottleneck that captures essential features in a reduced dimensionality [33].

In this study, we implemented a custom architecture that combines elements of a Convolutional Autoencoder (CAE) with those of a Denoising Autoencoder (DAE), tailored specifically for the analysis of neuronal calcium fluorescence traces. The denoising component is trained to recover clean signals from deliberately corrupted inputs, typically by introducing stochastic noise during training [34]. Whereas, the convolutional component, uses one-dimensional convolutional layers to capture local temporal patterns, such as spike events [35].

For training, a random subsample of 100 ROIs was selected per experimental condition. Of these, 80% were used for training and 20% for validation. This configuration enabled the model to learn underlying patterns in the activity traces while effectively filtering out experimental noise. An example of the reconstruction performance is shown in Fig. 4.

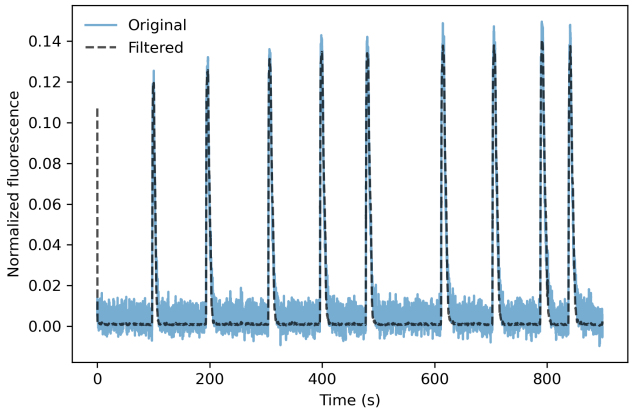

FIG. 4. Representative reconstructed fluorescence trace following autoencoder training. The original experimental data is shown as a solid blue line, while the corresponding reconstruction is depicted as a dashed black line.

F. Dimensionality reduction: t-SNE

t-distributed Stochastic Neighbor Embedding (t-SNE) is a non-linear dimensionality reduction technique specifically designed for the visualization of high dimensionality data. The goal of dimensionality reduction is to project high-dimensional data into a two- or three-dimensional space while preserving as much of the meaningful structure as possible, particularly local relationships between data points [36].

t-SNE is a variation of the earlier Stochastic Neighbor Embedding (SNE) algorithm. It consists of two main stages. Firstly, in the high-dimensionality space, for each pair of data points, the algorithm defines a conditional probability $p_{j|i}$ that a point x_i would pick x_j as its neighbor, assuming a Gaussian distribution centered at x_i with bandwidth σ_i:

$$p_{j|i} = \frac{\exp\left(-\|x_i - x_j\|^2 / 2\sigma_i^2\right)}{\sum_{k \neq i} \exp\left(-\|x_i - x_k\|^2 / 2\sigma_i^2\right)}. \tag{6}$$

These probabilities are then symmetrized into joint probabilities:

$$p_{ij} = \frac{p_{j|i} + p_{i|j}}{2n}, \tag{7}$$

where n is the total number of data points. The bandwidth σ_i is not fixed but adjusted to match a user-defined parameter known as *perplexity*, which controls the effective number of neighbors considered relevant for each point. The perplexity is defined in terms of the Shannon entropy (H) of P_i:

$$\text{Perp}(P_i) = 2^{H(P_i)}, \tag{8}$$

where $H(P_i) = -\sum_j p_{j|i} \log_2 p_{j|i}$. Then, in the low-dimensional space, the similarity between the corresponding points y_i and y_j is modeled using a Student's t-distribution with one degree of freedom (equivalent to a Cauchy distribution), which has heavier tails than a Gaussian:

$$q_{ij} = \frac{(1 + \|y_i - y_j\|^2)^{-1}}{\sum_{k \neq l} (1 + \|y_k - y_l\|^2)^{-1}}. \tag{9}$$

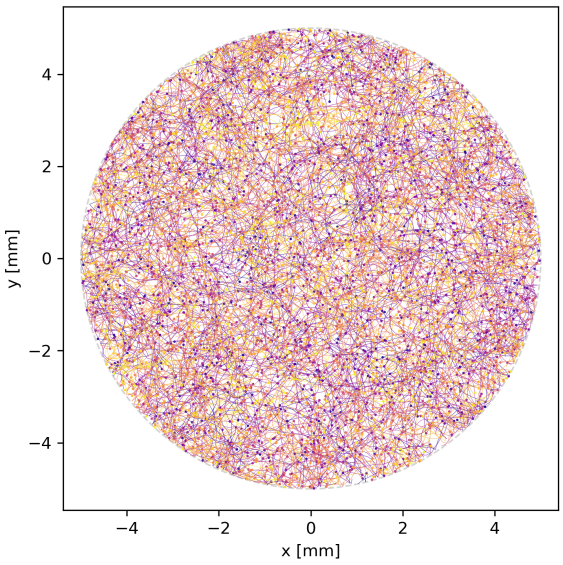

FIG. 5. Example of a biologically realistic structural network built *in silico* to resemble *in vitro* conditions.

This heavy-tailed distribution alleviates the 'crowding problem', i.e. the tendency for moderate-to-distant points to be mapped too closely together, by allowing moderate distances to remain distinguishable in the low-dimensional space.

Finally, the algorithm seeks to match the high-dimensional and low-dimensional similarities by minimizing the Kullback-Leibler (KL) divergence between the two distributions:

$$C = \sum_i \sum_j p_{ij} \log\left(\frac{p_{ij}}{q_{ij}}\right). \tag{10}$$

This cost function is minimized using stochastic gradient descent.

In summary, t-SNE creates a low-dimensional representation of data that preserves local similarities using probabilistic neighbor comparisons in both high- and low-dimensional spaces. The choice of perplexity is crucial: low values emphasize finer local structure, while high values consider broader relationships.

IV. *IN SILICO* MODEL

A. Biologically realistic neural networks

In order to simulate *in vitro* neuronal cultures in a biologically realistic manner, the network was constructed by replicating key aspects of neuronal development and connectivity observed experimentally [37].

Firstly, we placed $N = 5000$ neurons homogeneously and randomly on a circle of $R = 5$ mm in radius, representing the culture area. From each soma (neuron body), a single axon emerged with its initial orientation randomly assigned. Axonal growth was then modeled as a biased random walk designed to generate quasi-linear trajectories. Each axon's total length was sampled from a Rayleigh distribution with a mean value of $\langle l \rangle = 1.1$ mm, and was divided into 100 μm segments. At each growth step, the orientation of the new segment was modified relative to the previous one following a normal distribution with $\mu_\theta = 0°$ and $\sigma_\theta = 15°$. When an axon encountered the boundary of the defined culture, it bounced elastically against the wall, preserving the segment length and adjusting direction accordingly. A representative *in silico* structural positioning of axons is provided in Fig. 5.

Each neuron was also assigned a circular dendritic field centered on its soma, representing its area of influence. The diameter was drawn from a normal distribution with $\mu_d = 0.8$ mm and $\sigma_\theta = 0.05$ mm. Finally, connectivity was established based on spatial proximity. If an axon from the i-th neuron intersected the dendritic tree of the j-th neuron, a directed connection from $i \to j$ was formed. All connections were stored in a binary adjacency matrix $\mathbf{S} = \{s_{ij}\}$, where $s_{ij} = 1$ indicates a directed synapse from neuron i to neuron j, and $s_{ij} = 0$ otherwise.

B. Izhikevich model

The Izhikevich model [38] provides a computationally efficient yet biologically realistic description of neuronal dynamics, capable of reproducing a wide range of spiking and bursting behaviors observed in cortical neurons. The model is defined by the following two-dimensional system of ordinary differential equations:

$$\frac{dv}{dt} = 0.04v^2 + 5v + 140 - u + I, \tag{11}$$

$$\frac{du}{dt} = a(bv - u). \tag{12}$$

Here, v denotes the membrane potential of the neuron, and u is a recovery variable that accounts for the activation of K^+ ionic currents and inactivation of Na^+ ionic currents. The external drive or synaptic input currents is represented by I. When the membrane potential reaches a threshold of $v \geq 30$ mV, a spike (action potential) is elicited, and the variables are reset according to:

$$\text{if } v \geq 30 \text{ mV, then } \begin{cases} v \leftarrow c \\ u \leftarrow u + d. \end{cases} \tag{13}$$

The parameters a, b, c and d ensure the model can reproduce various electrophysiological firing patterns of cortical neurons: regular-spiking, intrinsically bursting, and chattering, among others. At the onset of simulation, all neurons are initialized with a resting membrane potential of -65 mV. Network dynamics can be driven by adding a noise term η in I ($I \to I + \eta$) or by applying

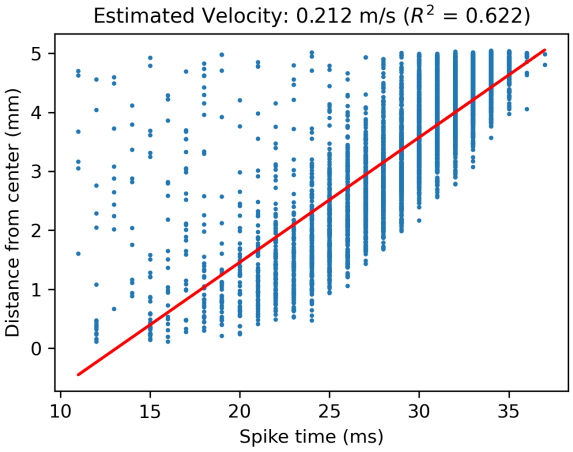

FIG. 6. Velocity analysis in numerical simulations. The plot shows the distance from the origin of activity to the front as a function of time with its corresponding linear regression for an induced bursting event. The resulting front propagation velocity is of 0.212 m/s and its corresponding $R^2 = 0.622$.

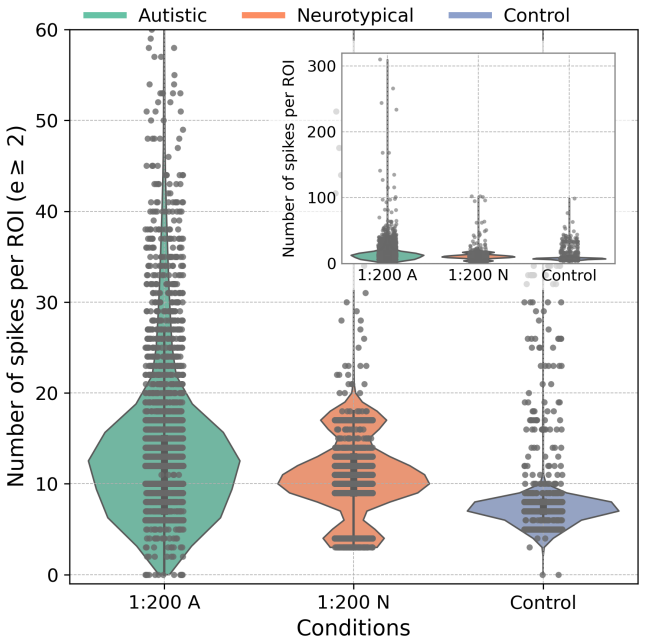

FIG. 7. Quantification of spike counts per ROI across the entire duration of 15-minute recordings in neuronal cultures at DIV 7, prepared under three experimental conditions. From left to right: autistic- treated cultures, neurotypical-treated cultures, and untreated control cultures (no fecal sample). The main plot shows the range of most of the data, and the inset the full range of values in the data. In all cases, the provided data has been generated by pooling together the results from $n = 5$ replicates for autistic and neurotypical cultures and $n = 6$ for controls.

a given stimulation. In our case, to generate a network activation and quantify its propagation velocity, a momentary external stimulus ($I = 50$ mV) is applied to a small subset of excitatory neurons located at the center of the network, eliciting an initial spike. Subsequently, these activated neurons influence their postsynaptic targets via synaptic interactions encoded in the input current I, potentially triggering further activity propagation through the network.

Following stimulation of the culture and the induction of a global firing event, propagation velocity was quantified. Consistent with the approach used for *in vitro* recordings, velocity was calculated by dividing the Euclidean distance of each region of interest (ROI) from the stimulation site by its corresponding activation time (Fig. 6). We note that, in general, it is difficult to precisely match the timescales of the numerical simulations with the experimental ones. For this reason, the velocities measured in simulations are about 10 times higher than those observed experimentally. For the sake of this investigation, we were interested in qualitative similarities or differences between simulations and experiments rather than a precise quantitative agreement.

V. RESULTS AND DISCUSSION

In this study, three experimental conditions were examined, each representing a distinct scenario: cultures modeling autism spectrum disorder (A), cultures modeling neurotypical conditions (N) and control (C) cultures. The results are organized into four main sections: (i) activity-related metrics, (ii) network structural properties, (iii) dimensionality reduction via t-SNE, and (iv) outcomes from computational simulations.

A. Activity descriptors

The raster plots, temporal activation patterns, and spatiotemporal organization of neuronal activity exhibited comparable features across conditions. Both control and treated cultures displayed episodes of pronounced synchronous activity, during which nearly all ROIs were simultaneously activated in the form of *bursts*, followed by periods of minimal activity (as in Fig. 2). This dynamic reflects an overall on–off pattern of network behavior, and will be treated in more detail later.

An additional approach to characterize the dynamics of the cultures is to examine the distribution of activity across all ROIs. Fig. 7 presents a violin plot showing the number of firing events for each of the 989 ROIs. Given that the activity threshold was set at a minimum of $e \geq 2$ spikes, no ROIs exhibit a firing count of $e = 1$. In control cultures, the majority of ROIs fired between 7 and 8 times per recording, with a small subset of highly active, noisy ROIs reaching up to 100 spikes. In neurotypically treated cultures, a slightly higher mode is observed around 10 spikes per recording, along with a secondary, smaller peak at approximately 17 spikes. Similar to controls, a few ROIs in this group also exhibited high-

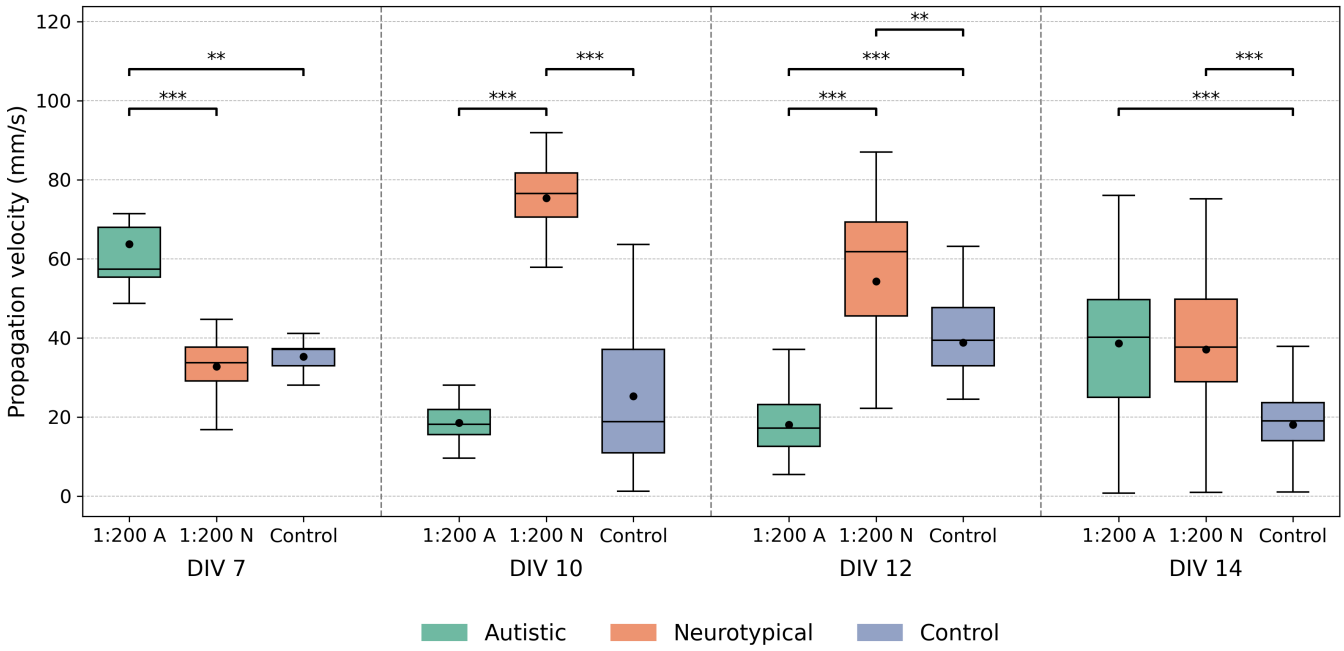

FIG. 8. Boxplots portraying the front propagation velocities in different culture groups (autistic, neurotypical, and control) over four days *in vitro*, corresponding to days 7, 10, 12, and 14 from left to right with statistical significance. Statistical difference is shown with symbols, where $^{*}p < 0.05$, $^{**}p < 0.01$ and $^{***}p < 0.001$ and its absence indicates no significance (Student's t-test). For clarity, only one experimental replicate is provided per condition, i.e., the same culture is monitored along different days and the different treatments compared. Black dots indicate the mean values for each dataset.

frequency firing up to 100 spikes. In contrast, autistic cultures showed a typical ROI firing rate centered around 13 spikes, along with an increase in both the frequency and amplitude of highly active ROIs. These findings suggest that autistic cultures exhibit more heterogeneous and elevated neuronal activity.

The front propagation velocities of bursting events (Fig. 8) exhibit a complex evolution throughout *in vitro* development. At DIV 7, corresponding to early stages of neuronal maturation, cultures are likely to be most influenced by pharmacological stress associated with initial metabolite damage. During this phase, autism-model cultures display significantly elevated mean propagation velocities ($\overline{v}_A \approx 63.68$ mm/s) compared to both neurotypical ($\overline{v}_N \approx 32.70$ mm/s) and control ($\overline{v}_C \approx 35.27$ mm/s) conditions, suggesting early alterations in network connectivity.

By DIV 10, the pattern shifts: neurotypical cultures begin to diverge from controls, while autistic and control cultures show comparable mean velocities, although the latter exhibit greater variability. Notably, this developmental window coincides with the onset of the "GABA switch" —a critical neurodevelopmental process whereby GABAergic signaling transitions from excitatory (depolarizing) to inhibitory (hyperpolarizing) action. This switch typically occurs between DIV 11 and DIV 13 in primary neuronal rat cultures [39, 40], and plays a fundamental role in establishing a finely tuned balance between excitation/inhibition (E/I). Disruptions to E/I balance have been implicated in several neurodevelopmental disorders, including autism [39].

At DIV 12, propagation velocities in autism-model cultures remain relatively stable, whereas control cultures exhibit a marked increase, potentially indicating an altered or delayed GABA switch in the autistic condition. By DIV 14, propagation velocities and their distributions converge between autistic and neurotypical conditions, while control cultures display reduced velocities with lower dispersion. This convergence may reflect activity-dependent plasticity mechanisms that partially normalize network function over time.

B. Connectivity descriptors

As previously described, several network-level descriptors were calculated from the effective connectivity matrices obtained via transfer entropy analysis. Representative examples for each experimental condition are shown in Fig. 9.

The developmental trajectories of three key graph-theoretical metrics, modularity (Q), global efficiency (G_{eff}), and average node degree ($\langle k \rangle$), are shown in Fig. 10. No statistically significant differences were detected between experimental conditions or across developmental stages. However, several noteworthy patterns emerge. Modularity tends to be higher in autistic-treated cultures between DIV 10 and DIV 12, whereas control

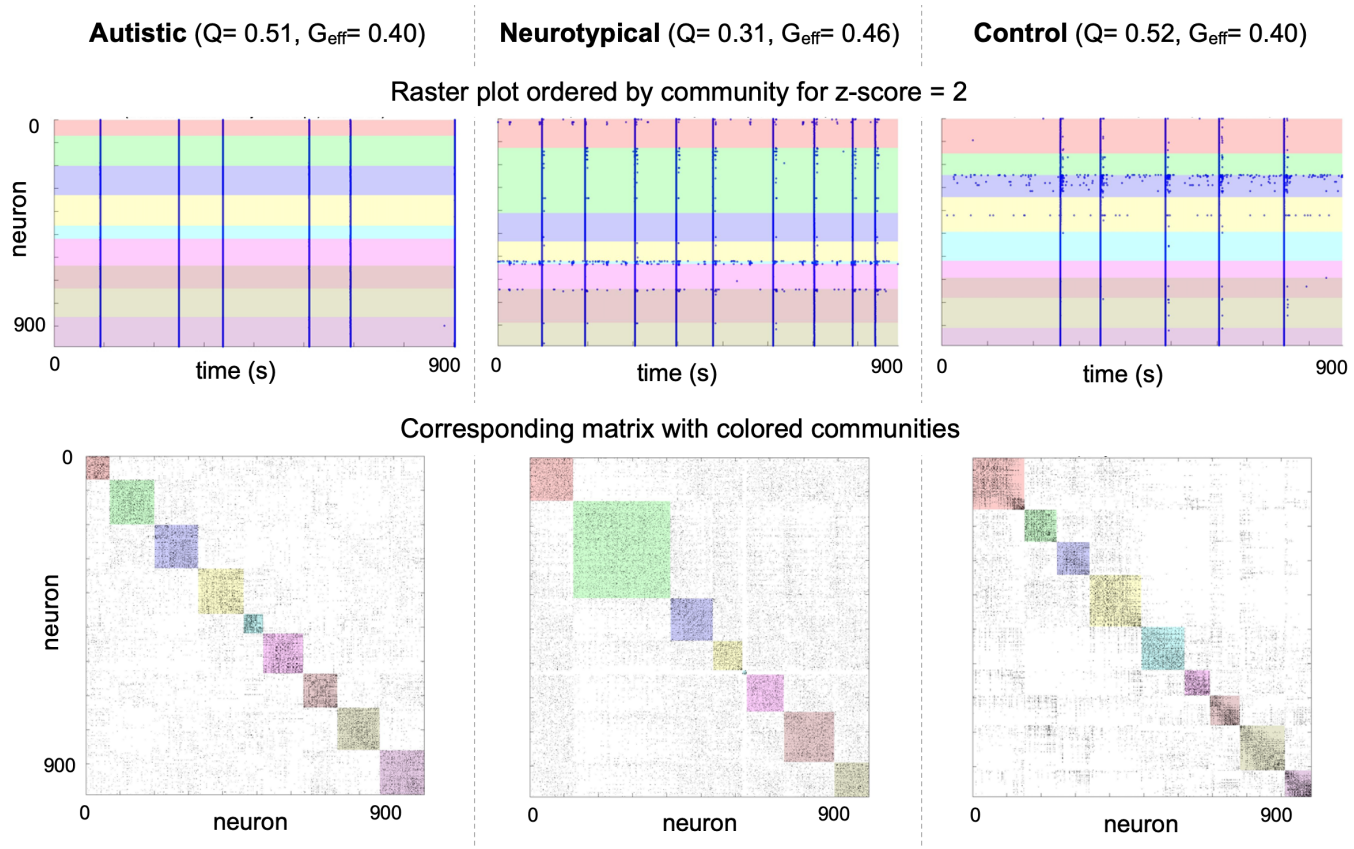

FIG. 9. Raster plots of activity for the 3 different experimental conditions at DIV 7, ordered by community for a z-score of 2 (top) with their corresponding effective connectivity matrices colored by communities (bottom). The resulting modularity and global efficiency values are shown for each of the cases.

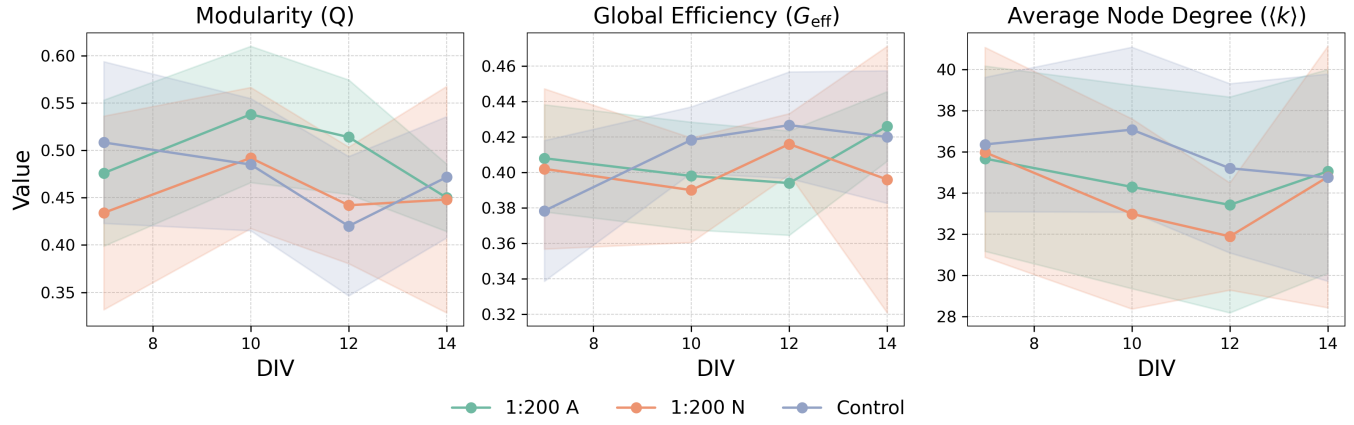

FIG. 10. Network metrics along development, from left to right: modularity (Q), global efficiency (G_{eff}) and average node degree, ($\langle k \rangle$)), where shaded areas represent their corresponding standard error for the three experimental conditions: autistic (A), neurotypical (N) and control (C) cultures. The number of replicates is $n = 5$ for autistic and neurotypical cultures and $n = 6$ for controls.

cultures exhibit slightly higher modularity values at DIV 7 and again at DIV 14. Global efficiency increases progressively in control networks over time, followed by a slight decline at the final time point. In contrast, both neurotypical and autistic cultures show an initial drop in global efficiency from DIV 7 to DIV 10. From there, their trajectories diverge: neurotypical cultures display a peak at DIV 12 followed by a decrease, while autistic networks continue to decline before exhibiting a modest rise at DIV 14. By this stage, global efficiency surpasses

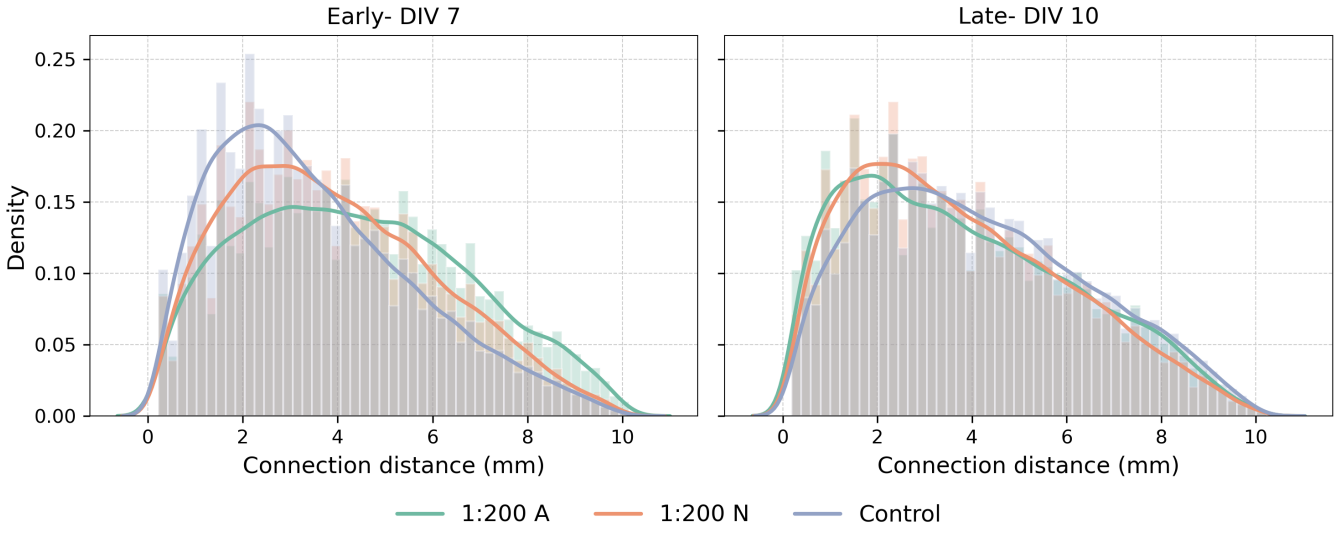

FIG. 11. Histogram of the distribution of connection distances within the culture in mm at two times in development, early- DIV 7 (left) and late- DIV 10 (right) with the corresponding probability density for the three experimental conditions: autistic (A), neurotypical (N) and control (C) cultures. For clarity, only one experimental replicate is provided per condition, i.e., the same culture is monitored along different days and the different treatments compared.

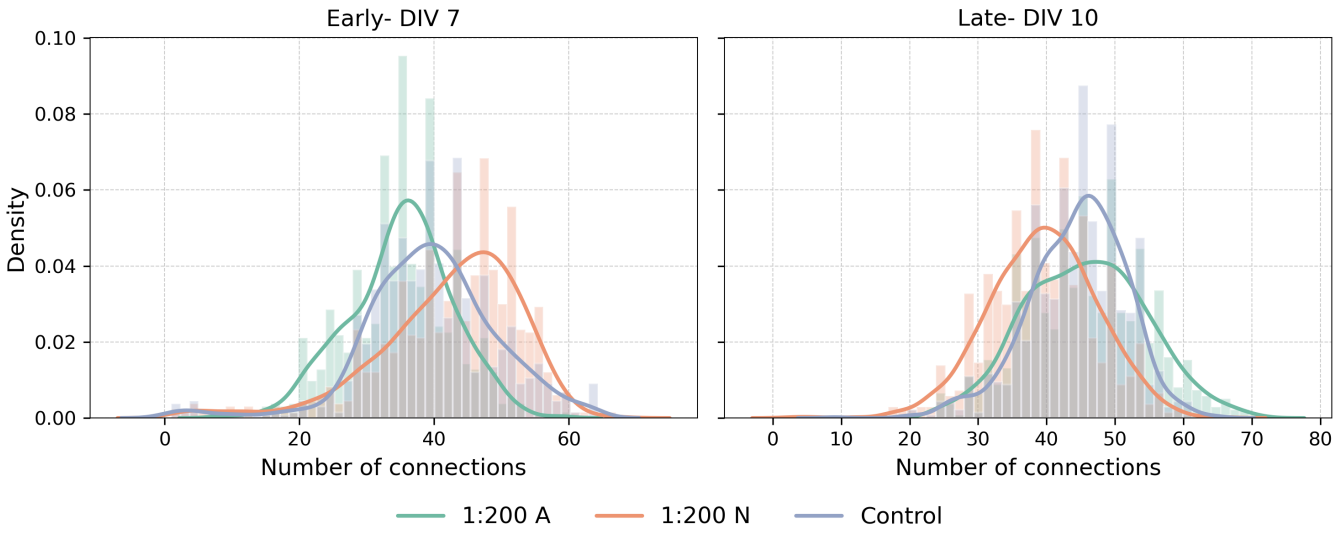

FIG. 12. Histogram of the distribution of the number of connections within the culture at two times in development, early- DIV 7 (left) and late- DIV 10 (right) with the corresponding probability density for the three experimental conditions: autistic (A), neurotypical (N) and control (C) cultures. For clarity, only one experimental replicate is provided per condition, i.e., the same culture is monitored along different days and the different treatments compared.

control levels in the autism-model condition but remains lower in the neurotypical group. The average node degree shows considerable variability, yet a general reduction in connectivity is evident in both neurotypical and autism-model cultures for DIV 10 and 12. Despite this, all three conditions converge to nearly identical values at the initial and final time points.

At the earliest developmental stage examined (DIV 7), both control and neurotypical cultures exhibit characteristic connection distances centered around $d \approx 2$ mm as shown in Fig. 11. The corresponding probability distributions are sharply peaked and rapidly decay, with very few connections extending beyond 8 mm, a trend particularly pronounced in control cultures. In contrast, the distribution of connection distances in autistic cultures differs substantially. Rather than displaying a distinct peak, these cultures exhibit a plateau spanning approximately 3 mm $\leq d \leq$ 5 mm, followed by a gradual decline.

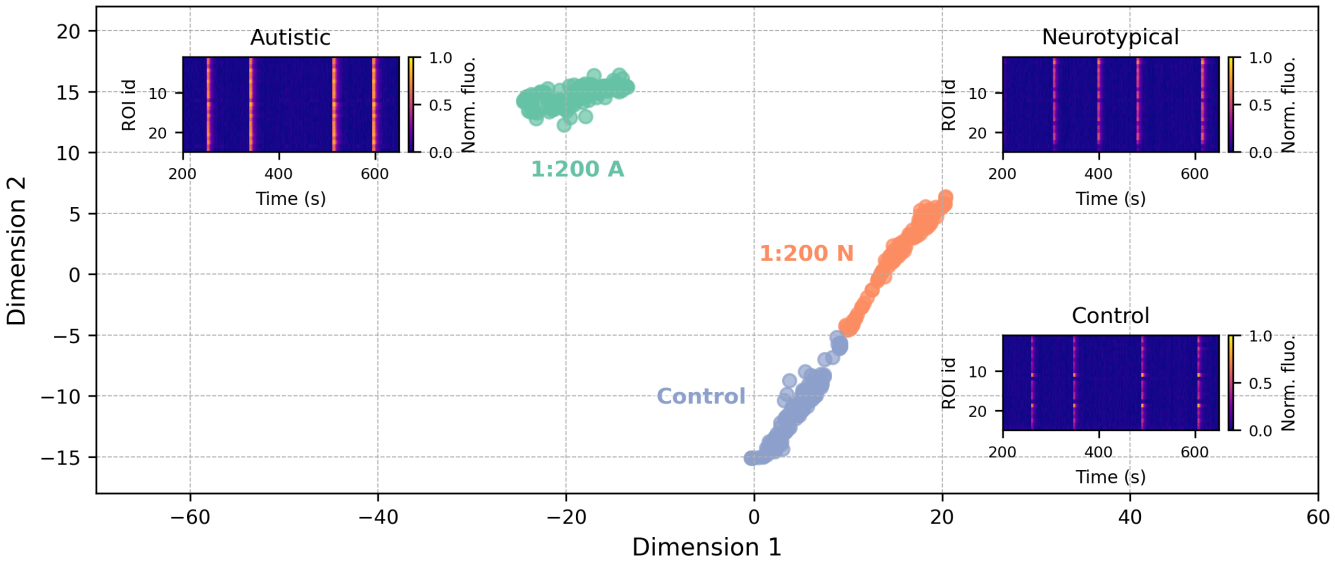

FIG. 13. t-SNE for a subsample of 100 ROIs (colored data clouds) for each condition at day *in vitro* 7 with its corresponding fluorescence activity map. The fluorescence map shows the normalized fluorescence for a subsample of 25 ROIs for 450s for each condition.

This pattern suggests a relative enrichment of mid- to long-range connections in immature autistic-treated networks, in comparison to their control and neurotypical counterparts.

By DIV 10, this distinctive profile is no longer observed; the distributions of connection distances converge across all conditions. Interestingly, at this stage, autism-model cultures display slightly shorter-range connections than the other two groups.

Connection density per ROI provides additional insight into the organization of these networks (Fig. 12). At DIV 7, the autistic group exhibits a narrower distribution centered around 35 connections per ROI, reflecting lower overall connectivity. Moreover, a subset of ROIs in these cultures displays unusual sparse connectivity, with fewer than 25 connections. In comparison, control and neurotypical distributions are centered at approximately 40 and 49 connections per ROI, respectively, with neurotypical cultures exhibiting higher connectivity overall. As development progresses, the number of connections in autism-model cultures increases, reaching approximately 48 by DIV 14, comparable to control levels (46 connections), while neurotypical cultures show a modest decline to around 40 connections per ROI.

Collectively, these findings suggest that networks resulting from cultures treated with autistic-derived metabolites initially form fewer but longer-range connections, accompanied by greater heterogeneity in connectivity, which are partially normalized as the cultures mature.

C. t-SNE

Raw fluorescence traces were processed through an autoencoder trained to capture the intrinsic activity patterns while minimizing experimental noise. Following this reconstruction step, dimensionality reduction using t-SNE was applied. As shown in Fig. 13, control and neurotypical cultures tended to cluster in close proximity, whereas the autistic case shaped a distinctly separate group. Given that t-SNE is designed to preserve local distances from the high-dimensional space in the lower-dimensional representation, this separation indicates meaningful differences in the underlying fluorescence dynamics across conditions.

Since fluorescence data reflects the dynamics of the neurons, these results suggest the presence of distinct activity patterns in autism-model networks. Indeed, when analyzing the normalized fluorescence signals directly, as opposed to a binarized representation, it becomes evident that autism-model cultures often reach higher fluorescence intensities compared to both neurotypical and control samples, indicating larger burst amplitudes. Further investigation is warranted to determine whether this behavior is consistent across experimental replicates and whether it reflects altered excitability or network synchronization in these cultures.

Figure 14 illustrates the developmental trajectories in phase space for each experimental condition, spanning from DIV 7 to DIV 14. Notably, DIV 7 appears to exhibit the strongest effect of the metabolites, as reflected in the pronounced separation between control and autistic cultures at this stage, with neurotypical networks occupying an intermediate position. Control cultures follow the

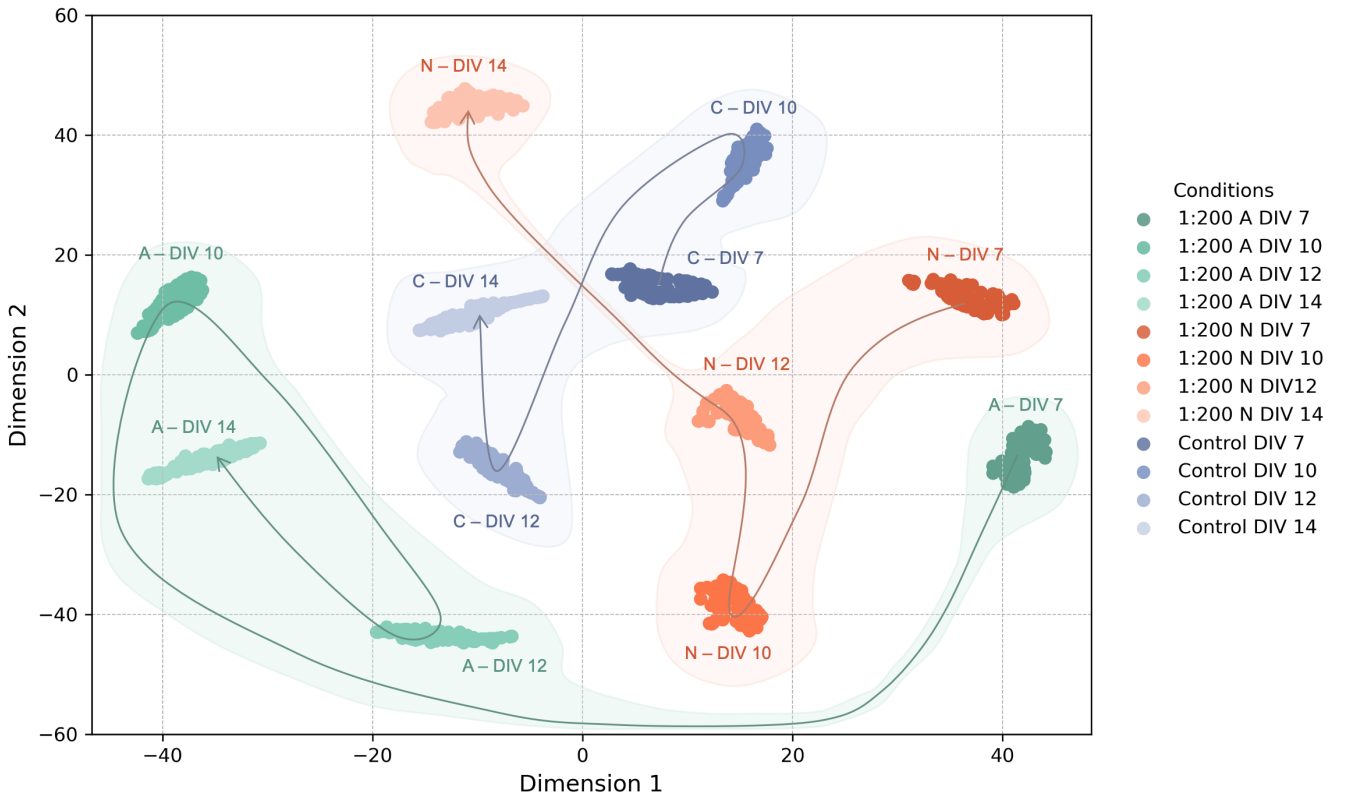

FIG. 14. t-SNE for a subsample of 100 ROIs (colored data clouds) for the three experimental conditions: autistic (A), neurotypical (N) and control (C) cultures, along development, at DIV 7, 10, 12, and 14. Arrows indicate the temporal trajectory of each condition through the phase space.

most compact trajectory, remaining largely confined near the center of the projection. Neurotypical samples form a nearby cluster, initially positioned toward the lower right of the phase space at DIV 7, 10, and 12, and shifting toward the upper left by DIV 14. In contrast, autism-model cultures exhibit the largest displacement between DIV 7 and DIV 10, suggesting that the most prominent differences in network activity may emerge during the early stages of development, as suspected. From DIV 10 to 14, the trajectory of autistic cultures becomes more localized, with smaller shifts in position, ultimately stabilizing in the lower left region relative to the control cluster.

D. *In silico* simulations

To complement the experimental findings, *in silico* simulations were conducted with the aim of reproducing key dynamical features observed in the biological data. Specifically, the objective was to investigate whether increased front propagation velocities could arise in networks with reduced connection density, provided those connections were predominantly long-range.

Figure 15 presents a heatmap illustrating the impact of average connection number (x-axis) and mean axonal length (y-axis) on propagation velocity. The upper-left quadrant of the plot corresponds to conditions resembling control cultures, characterized by high connectivity and relatively short average axonal lengths ($\langle l \rangle = 1.1$ mm), consistent with experimental observations. In contrast, the lower-right region of the heatmap reflects a regime with reduced connectivity but extended axonal projections, an architecture representative of the autistic condition in the experimental data. Propagation velocities in the former scenario are approximately 0.25 m/s, whereas in the latter they exceed 0.35 m/s. These results indicate that increased propagation velocity can be achieved in networks with sparser connectivity when connections are longer-range. This graph highlights the intricate relationship between network connectivity and propagation dynamics, demonstrating that velocity is influenced by several factors such as number of connections and their spatial distribution, among others.

These simulations demonstrate that the Izhikevich neuronal network model can replicate key dynamic behaviors of the cultures, notably elevated propagation velocities, by modulating structural features inferred from effective connectivity analyses. This suggests that differences in connection density and spatial reach can account

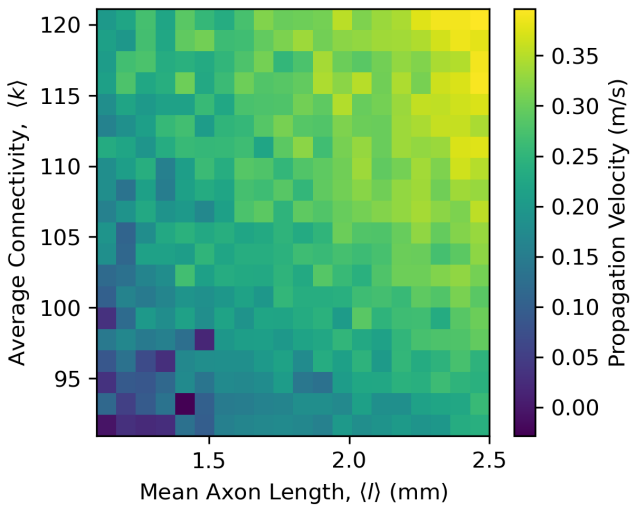

FIG. 15. Heatmap of propagation velocities (m/s) of stimulation-generated activity fronts, as a function of average network connectivity, $\langle k \rangle$, and mean axonal length, $\langle l \rangle$, used in network construction.

for observed functional disparities across experimental groups. It is important to note that the temporal scale is not adjusted to biologically-realistic times because in this scenario equations become much more complex, and we are interested in a qualitative analysis rather than a quantitative one.

VI. CONCLUSIONS

This study investigated the influence of autism spectrum disorder-associated metabolites on neuronal network development and dynamics, with the aim of gaining insight into their potential role in the causation and pathophysiology of ASD.

Experimental findings revealed notable differences in the early stages of culture development. At the dynamic level, cultures treated with ASD-related metabolites exhibited more dispersed activity and significantly faster front propagation velocities compared to neurotypical and control conditions. While no statistically significant differences were found across groups in global network metrics such as modularity, global efficiency, or average node degree, it was observed that neurotypical-treated cultures deviated most from control behavior in these parameters. Importantly, a more detailed analysis of network topology revealed that ASD-treated cultures tended to form fewer connections per ROI, with those connections extending over longer distances, a distinctive feature not observed in the other conditions.

Further support for these findings came from dimensionality reduction techniques applied to raw fluorescence data, which consistently segregated ASD-treated cultures from neurotypical and control groups in the low-dimensional space. This separation suggests inherent differences in the underlying activity patterns. Additionally, *in silico* modeling using the Izhikevich framework confirmed that elevated propagation velocities can emerge in sparsely connected networks, provided those connections span longer distances, mirroring the structural characteristics observed experimentally.

Overall, these results contribute to a deeper understanding of how ASD-associated biochemical environments may impact the development and functional organization of neuronal networks. Continued experimental efforts will be essential to fully elucidate the mechanisms at play and validate these observations across broader models and conditions.

ACKNOWLEDGMENTS

I would like to express my sincere gratitude to my supervisor, Dr. Jordi Soriano Fradera, for his invaluable guidance, continuous support, and scientific insight throughout the development of this project. His dedication to research and genuine enthusiasm for science have been truly motivating and instrumental in shaping this work.

I am also deeply thankful to Dr. Rosa Del Campo, Dr. Javier Galeano, Dr. José Avendaño Ortiz, and Dr. Jesús Gómez Gardeñes for their essential contributions and thoughtful input, which played a key role in the successful completion of this study. In particular, I wish to thank Dr. Rosa Del Campo and Dr. José Avendaño Ortiz for providing the biological samples from the Instituto Ramón y Cajal de Investigación Sanitaria, without which this research would not have been possible.

My appreciation also goes to PhD students Mireia Olives and Mikel Ocio for their collaboration, technical assistance, and constant support during the project.

Lastly, I am profoundly grateful to my family and friends for their patience, encouragement, and unwavering support throughout this academic journey. Your belief in me has been a constant source of strength.

[1] Lord, C., Brugha, T., Charman, T., Cusack, J., Dumas, G., Frazier, T., Jones, E., Jones, R., Pickles, A., State, M. & Others "Autism spectrum disorder", *Nature Reviews Disease Primers*. vol. 6, pp. 5, 2020.

[2] Won, H., Mah, W. & Kim, E. "Autism spectrum disorder causes, mechanisms, and treatments: focus on neuronal synapses", *Frontiers In Molecular Neuroscience*, vol. 6 pp. 19, 2013.

[3] Monk, C., Peltier, S., Wiggins, J., Weng, S., Carrasco, M., Risi, S. & Lord, C. "Abnormalities of intrinsic func-

tional connectivity in autism spectrum disorders", *Neuroimage*. vol. 47, pp. 764-772, 2009.

[4] Lord, C., Elsabbagh, M., Baird, G. & Veenstra-Vanderweele, J. "Autism spectrum disorder", *The Lancet*, vol. 392, pp. 508-520, 2018.

[5] Ma, C., Li, W., Ke, S., Lv, J., Zhou, T. & Zou, L. "Identification of autism spectrum disorder using multiple functional connectivity-based graph convolutional network", *Medical & Biological Engineering & Computing*, vol. 62, pp. 2133-2144, 2024.

[6] Rane, P., Cochran, D., Hodge, S., Haselgrove, C., Kennedy, D. & Frazier, J. "Connectivity in autism: a review of MRI connectivity studies", *Harvard Review Of Psychiatry*, vol. 23, pp. 223-244, 2015.

[7] Hull, J., Dokovna, L., Jacokes, Z., Torgerson, C., Irimia, A. & Van Horn, J. "Resting-state functional connectivity in autism spectrum disorders: a review", *Frontiers In Psychiatry*, vol. 7, pp. 205, 2017.

[8] Cerliani, L., Mennes, M., Thomas, R., Di Martino, A., Thioux, M. & Keysers, C. "Increased functional connectivity between subcortical and cortical resting-state networks in autism spectrum disorder", *JAMA Psychiatry*, vol. 72, pp. 767-777, 2015.

[9] Roe, K. "Autism spectrum disorder initiation by inflammation-facilitated neurotoxin transport", *Neurochemical Research*. 47, 1150-1165, 2022.

[10] Kuziel, G. & Rakoff-Nahoum, S. "The gut microbiome", *Current Biology*, vol. 32, pp. R257-R264, 2022.

[11] Douglas, A. "Fundamentals of microbiome science: how microbes shape animal biology", Princeton University Press, 2018.

[12] Gwak, M. & Chang, S. "Gut-brain connection: microbiome, gut barrier, and environmental sensors", *Immune Network*, vol. 21, pp. e20, 2021.

[13] Gwak, M. & Chang, S. "Gut-brain connection: microbiome, gut barrier, and environmental sensors", *Immune Network*, vol. 21, pp. e20, 2021.

[14] Roe, K. "Autism spectrum disorder initiation by inflammation-facilitated neurotoxin transport", *Neurochemical Research*, vol. 47, pp. 1150-1165, 2022.

[15] Gordon, J. & Amini, S. "General overview of neuronal cell culture", *Neuronal Cell Culture: Methods And Protocols*. pp. 1-8, 2021.

[16] Soriano, J. "Neuronal cultures: Exploring biophysics, complex systems, and medicine in a dish." *Biophysica*. 3, 181-202, 2023.

[17] Millet, L. & Gillette, M. "Over a century of neuron culture: from the hanging drop to microfluidic devices", *The Yale Journal Of Biology And Medicine*. vol. 85, pp. 501, 2012.

[18] Douglas, A. *Fundamentals of microbiome science: how microbes shape animal biology*, Princeton University Press, 2018.

[19] Xiong, L., Chen, P. & Zhou, Q. "Adhesion promotion between PDMS and glass by oxygen plasma pre-treatment", *Journal Of Adhesion Science And Technology*. vol. 28, pp. 1046-1054, 2014.

[20] Kim, Y., Baek, N., Han, Y., Chung, M. & Jung, S. "Enhancement of neuronal cell adhesion by covalent binding of poly-D-lysine." *Journal Of Neuroscience Methods*. 202, 38-44, 2011.

[21] Park, G., Kim, S., Shim, J. & Lee, S. "Brief guide to immunostaining", *Molecules And Cells*, vol. 48, pp. 100157, 2025.

[22] Zhang, Y. & Looger, L. "Fast and sensitive GCaMP calcium indicators for neuronal imaging", *The Journal Of Physiology*, vol. 602, pp. 1595-1604, 2024.

[23] Orlandi, J., Fernández-García, S., Comella-Bolla, A., Masana, M., Barriga, G., Yaghoubi, M., Kipp, A., Canals, J., Colicos, M., Davidsen, J. & Others "NETCAL: an interactive platform for large-scale, NETwork and population dynamics analysis of CALcium imaging recordings", *Neuroscience*, vol. 10, 2017.

[24] Jacobi, S., Soriano, J. & Moses, E. "BDNF and NT-3 increase velocity of activity front propagation in unidimensional hippocampal cultures", *Journal Of Neurophysiology*, vol. 104, pp. 2932-2939, 2010.

[25] Montalà-Flaquer, M., López-León, C., Tornero, D., Houben, A., Fardet, T., Monceau, P., Bottani, S. & Soriano, J. "Rich dynamics and functional organization on topographically designed neuronal networks in vitro", *Iscience*, vol. 25, 2022.

[26] Stiso, J. & Bassett, D. "Spatial embedding imposes constraints on neuronal network architectures", *Trends In Cognitive Sciences*, vol. 22, pp. 1127-1142, 2018.

[27] Vicente, R., Wibral, M., Lindner, M. & Pipa, G. "Transfer entropy—a model-free measure of effective connectivity for the neurosciences", *Journal Of Computational Neuroscience*, vol. 30, pp. 45-67, 2011.

[28] Rubinov, M. & Sporns, O. "Complex network measures of brain connectivity: uses and interpretations", *Neuroimage*, vol. 52, pp. 1059-1069, 2010.

[29] Newman, M. & Girvan, M. "Finding and evaluating community structure in networks", *Physical Review E*, vol. 69, pp. 026113, 2004.

[30] Newman, M. "Modularity and community structure in networks", *Proceedings Of The National Academy Of Sciences*, vol. 103, pp. 8577-8582, 2006.

[31] Fortunato, S. "Community detection in graphs", *Physics Reports*, vol. 486, pp. 75-174, 2010.

[32] Boccaletti, S., Latora, V., Moreno, Y., Chavez, M. & Hwang, D. "Complex networks: Structure and dynamics", *Physics Reports*. vol. 424, pp. 175-308, 2006.

[33] Bank, D., Koenigstein, N. & Giryes, R. "Autoencoders", *Machine Learning For Data Science Handbook: Data Mining And Knowledge Discovery Handbook*, pp. 353-374, 2023.

[34] Vincent, P., Larochelle, H., Bengio, Y. & Manzagol, P. "Extracting and composing robust features with denoising autoencoders", *Proceedings Of The 25th International Conference On Machine Learning*, pp. 1096-1103, 2008.

[35] Masci, J., Meier, U., Cireşan, D. & Schmidhuber, J. "Stacked convolutional auto-encoders for hierarchical feature extraction", *Artificial Neural Networks And Machine Learning–ICANN 2011: 21st International Conference On Artificial Neural Networks, Espoo, Finland, June 14-17, 2011, Proceedings, Part I 21*, pp. 52-59, 2011.

[36] Maaten, L. & Hinton, G. "Visualizing data using t-SNE", *Journal Of Machine Learning Research*, vol 9, 2008.

[37] Orlandi, J., Soriano, J., Alvarez-Lacalle, E., Teller, S. & Casademunt, J. "Noise focusing and the emergence of coherent activity in neuronal cultures", *Nature Physics*, vol. 9, pp. 582-590, 2013.

[38] Izhikevich, E. "Simple model of spiking neurons", *IEEE Transactions On Neural Networks*, vol. 14, pp. 1569-1572, 2003.

[39] Leonzino, M., Busnelli, M., Antonucci, F., Verderio, C., Mazzanti, M. & Chini, B. "The timing of the excitatory-to-inhibitory GABA switch is regulated by the oxytocin receptor via KCC2", *Cell Reports*, bol. 15, pp. 96-103, 2016.

[40] Ganguly, K., Schinder, A., Wong, S. & Poo, M. "GABA itself promotes the developmental switch of neuronal GABAergic responses from excitation to inhibition", *Cell*, vol. 105, pp. 521-532, 2001.